

# Study of Structural Defects in Sapphire Ribbons using X-Ray Topography and Coherent Imaging in Synchrotron Radiation

T. S. Argunova<sup>a,\*</sup>, V. G. Kohn<sup>b</sup>, J.-H. Lim<sup>c</sup>, V. M. Krymov<sup>a</sup>, and S. Yu. Martyushov<sup>d</sup>

<sup>a</sup> Ioffe Physical—Technical Institute, Russian Academy of Sciences, St. Petersburg, 194021 Russia

<sup>b</sup> National Research Center “Kurchatov Institute”, Moscow, 123182 Russia

<sup>c</sup> Synchrotron Radiation Source “Pohang Light Source”, Pohang, 790-784 Republic of Korea

<sup>d</sup> Technological Institute of Superhard and New Carbon Materials, Troitsk, Moscow, 108840 Russia

\*e-mail: argunova@mail.ioffe.ru

Received June 26, 2023; revised August 10, 2023; accepted August 10, 2023

**Abstract**—The method of X-ray phase contrast has found wide application in coherent-synchrotron-radiation sources. In this study, this method is used in combination with X-ray diffraction topography to investigate structural defects and inhomogeneities in the volume of basal-faceted sapphire ribbons. The phase-contrast images of gas pores are analyzed in detail using computer simulation. X-ray topography methods are used to study the generation of dislocations by pores. The combination of methods provides information that is virtually impossible to obtain using traditional optical microscopy.

**Keywords:** sapphire, Stepanov’s method, gas pores, dislocations, synchrotron radiation, phase contrast, X-ray topography

**DOI:** 10.1134/S1027451023070030

## INTRODUCTION

It is known that when crystals grow from a melt supersaturated with dissolved gases, gas pores are formed in the crystals. These pores are formed in those places on the growth front, where gas bubbles are held by surface-tension forces, and crystal growth is hindered. Differences in the composition and shape of pores indicate the complexity of the processes leading to their formation. The issues of visualizing pores, the sizes of which range from submicron to several micrometers, are of scientific and practical interest.

Sapphire is a typical representative of crystals grown from a melt under a temperature gradient. It finds application in electronics, optics, medicine, and various fields of technology on account of a number of exceptional properties. In particular, being optically transparent over a wide range of wavelengths, sapphire scatters transmitted radiation and becomes unsuitable for optical applications at high concentrations of pores. Another important problem is that the nonuniform distribution of thermoelastic stresses over a growing crystal gives rise to plastic deformation [1]. In this case, the pores play the role of stress concentrators and can cause the generation of dislocations [2]. As a result of the interaction and rearrangement of dislocations, a block structure is formed [3] leading to a decrease in crack resistance. Thus, sapphire windows operating in a wide range of pressures and tempera-

tures lose not only their transparency, but also their strength.

The set of reasons for the appearance of micropores in profiled sapphire crystals grown by Stepanov’s method is described in a large number of works, for example, [4–6]. Since these crystals grow from a thin layer of melt under conditions of complex hydrodynamics of flows, they are characterized by a surface layer containing an increased density of pores. In particular, the ribbons used for making windows need require the surface layer of pores to be removed by grinding and polishing. At the same time, ribbons with an atomically smooth basal face could be used in the “as grown” state not only for windows, but also as substrates for microelectronic structures.

Owing to the widespread use of sapphire products, researchers pay great attention to its study. However, some problems that arise when growing basal-faceted ribbons have remained unsolved. For example, the model for the formation of a block structure [2, 3] is confirmed by calculating the distribution of thermal stresses over a growing crystal, but is not fully confirmed by the results of analyzing the types and geometry of dislocations. Having agreed with the role of pores as stress concentrators capable of causing plastic deformation, one has to admit that the problem of determining the characteristics of such concentrators has not yet been solved.

Until recently, the main methods for imaging defects in sapphire were X-ray topography (XRT) [2, 3] and optical microscopy [1, 5, 6]. The relatively low resolution of optical microscopy does not allow one to see the details of the morphology of small pores. When detecting the latter, the short focal length of a high-magnification objective lens ( $\geq 100\times$ ) limits the use of a light microscope to very thin samples. On the other hand, in an X-ray projection topograph [7], the image of a pore is determined by elastic deformations in the part of the crystal surrounding the pore. In this case, already nucleated dislocations make a significant contribution to the contrast [2]. Imaging micron-sized pores is only possible with high sensitivity to slight violations in the crystal lattice. This condition is satisfied by two methods: plane-wave and sectional topography [8].

With the commissioning of synchrotron radiation (SR) sources, it became possible to use XRT methods in a wider range of  $\mu t$  values compared to an X-ray tube, where  $\mu$  is the radiation-absorption coefficient and  $t$  is the thickness of the sample. In the SR beam from an undulator, images (with a size from 10 to 40  $\mu\text{m}$ ) were obtained from small pores in both monochromatic and white SR [9, 10]. However, in the absence of computer-image simulation, determination of the actual pore size is often difficult. At the same time, the simulation results may be unexpected. Taking the model of a spherical pore in a perfect crystal as a basis and calculating the bipartite black-and-white contrast caused by the deformation field around the pores in Al–Pd–Mn quasi-crystals, the authors discovered a discrepancy between the object and the model [11]. The pores, which had the appearance of roundness on the topographs, looked like projections of faceted objects on a phase-contrast image [11, 12].

This work is devoted to studying dislocations and micropores in samples of basal-faceted sapphire ribbons using synchrotron topography in combination with phase-contrast imaging. Transmission phase-contrast imaging [13] is a relatively new method that arose due to the unique properties of SR beams from the source of the third-generation ESRF (European Synchrotron Radiation Facility) in Grenoble, France [14]. To obtain the phase of the radiation wave field after its conversion to intensity, the high coherence of X-ray sources and high resolution of X-ray detectors are required. We use the above methods in combination with each other at one SR station with parameters that are significantly inferior to those of the ESRF synchrotron stations. Nevertheless, the combination of methods helps us to advance our understanding of the nature of structural defects and microinhomogeneities in profiled sapphire crystals.

## EXPERIMENTAL

A basal-faceted ribbon was grown from the melt using Stepanov's method at a growth rate of 1 mm/min up to a size of  $31 \times 1.3 \times 265$  ( $W \times H \times L$ )

mm<sup>3</sup>. The process was carried out in a specially designed thermal zone, where temperature gradients were controlled by heat shields. Adjustment and tuning of the position of the seed relative to the stretching device and the shaper was carried out using a laser. As a result, the misorientation of the ribbon surface relative to the basal facet was only a few arc minutes.

Examination of the ribbon using an optical microscope revealed that its growth surfaces had a slight relief without signs of a damaged layer. A block structure was observed in that part of it that was located at a distance of  $\sim 200$  mm from the seed. The sample was cut near the "neck" of the ribbon in the direction perpendicular to the growth axis and used for X-ray experiments without additional processing.

Numerous studies of dislocations in sapphire ribbons using the Lang projection method [7] were described earlier, for example, in [2, 3, 15]. The use of SR opens up new possibilities mainly on account of the fact that XRT and phase-contrast imaging (PCI) methods can be combined with each other. Figure 1a shows the principle of the PCI method. By placing the crystal at a large distance  $Z_0$  from the SR source, the experimenter obtains an image of micropores in the volume of the sample, since a microscopic change in thickness along the path of the rays leads to a noticeable phase shift of the coherent radiation passing through the sample. With increasing distance  $Z_1$ , the curvature of the phase front causes a nonuniform distribution of intensity, which can be measured using a detector.

The XRT and PCI methods combine well with each other at one SR station in radiation with a spatial coherence length on the order of several tens of microns. Figure 1b schematically shows the experimental setup for combined use of the methods. Radiation diffracted in crystal  $C$  installed at the Bragg reflection angle enters detector  $D_1$ . The detector  $D_2$  is designed for recording phase-contrast images. In our case, the experiments were carried out sequentially; in this case, in the PCI method, the surface of the ribbon was installed perpendicular to the beam. The distance  $Z_1$  ranged from a few millimeters to one meter.

It is known that at small distances  $Z_1$  between the detector and the sample, i.e., in the near field, the transverse size of the pore can be determined from the number of pixels in the image and the pixel size of the detector. The near-field condition is satisfied at  $2r_1 \ll D$ , where  $r_1 = (\lambda Z_1)^{1/2}$  is the radius of the first Fresnel zone for wavelength  $\lambda$  at a distance  $Z_1$  from a pore with diameter  $D$ . Moreover, if  $D$  does not exceed several micrometers, then correct estimate of the near-field limit will be approximately ten times less than  $Z_c$ , where  $Z_c$  corresponds to the value  $r_1 = D/2$ . For example, for a microtube with a diameter of  $D = \sim 2$   $\mu\text{m}$  and  $\lambda = 0.775$   $\text{\AA}$ ,  $Z_1 = 0.1$  cm [16]. In other words, in the near field,  $Z_1$  does not exceed a few millimeters. The

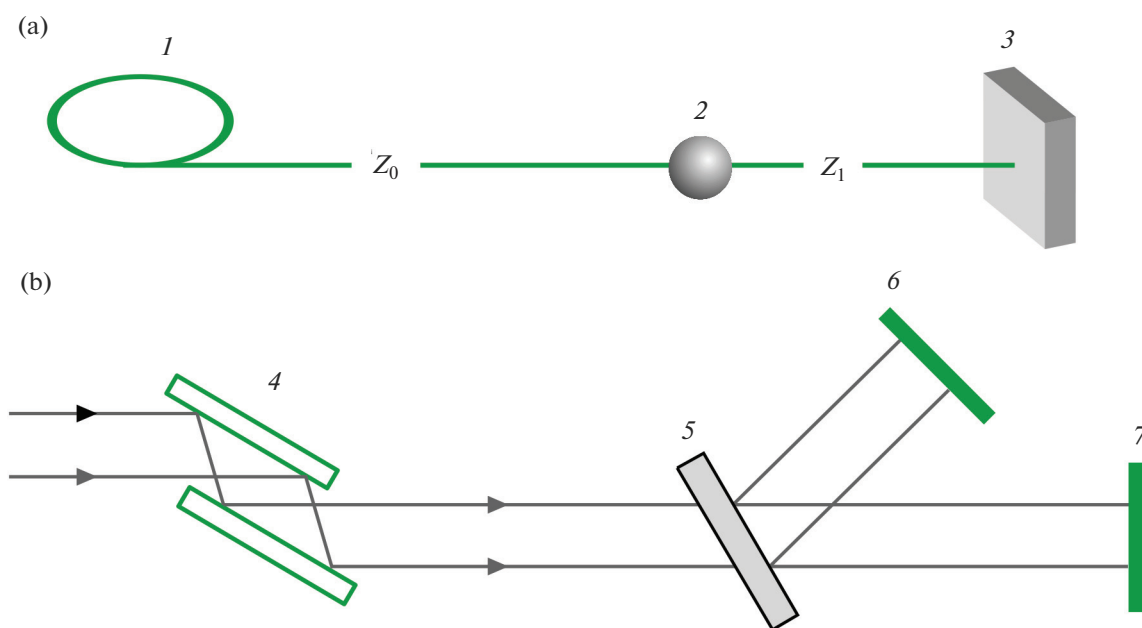


**Fig. 1.** (a) Scheme for obtaining phase-contrast images: (1) SR source, (2) object, and (3) detector;  $t \ll Z_1 \ll Z_0$ , where  $t$  is the thickness of the object;  $Z_1$  is the distance between the object and detector, and  $Z_0$  is the distance to the SR source. (b) Scheme of sequential recording of phase-contrast and X-ray topographic images at one station: (4) X-ray mirrors, (5) crystal sample, (6) detector for topography, and (7) detector for recording phase-contrast images.

limited resolution of the detector and the high level of parasitic noise do not allow the experimenter to measure the size of micropores in the near field. In the far field, when  $2r_1 \gg D$ , the image size increases and many Fresnel zones are formed. Therefore, to restore the real size of the micropores, it is necessary to solve the inverse problem by simulating their images.

The experiments were carried out at the Pohang Light Source (PLS) SR source in Pohang, South Korea. As a result of modernization undertaken in 2009–2011 to increase the SR intensity, the energy of electrons in the PLS accelerator ring was increased from 2.5 to 3.0 GeV. To carry out experiments in the high-energy range, a multipole wiggler was installed at station 6c “Biomedical Imaging.” Gas pores in sapphire crystals were studied by sequential application of the XRT and PCI methods at 6c station.

Bragg diffraction images were obtained in SR with an energy of 15 keV ( $\lambda = 0.827 \text{ \AA}$ ). Multilayer X-ray mirrors ( $\Delta E/E \approx 2\%$ ) based on Ru/C were used for monochromatization. Topographs were recorded using a two-coordinate detector, the basis of which is a charge-coupled device (CCD). The detector had a large field of view ( $64 \times 42 \text{ mm}^2$ ), high resolution ( $4008 \times 2571$  pixels), and a pixel size of  $16 \text{ \mu m}$  (VHR CCD Photonic science, St. Leonards-on-Sea, United Kingdom). A fine-grained Kodak M100 X-ray film was used to work out small details. The typical exposure times ranged from several tens to several seconds depending on the type of recording.

Phase-contrast images of micropores in monochromatic SR were recorded only on the detector. The Zyla CCD camera (Andor, Oxford Instruments, United Kingdom) had a resolution of  $2560 \times 2160$  pixels with a pixel size of  $6.5 \times 6.5 \text{ \mu m}^2$ . The field of view or maximum sample area covered in one exposure was  $16.6 \times 14.0 \text{ mm}^2$ . We note that, compared to other X-ray coherent imaging methods [17], the PCI method has a fairly large field of view, which allows comparisons with the XRT method. The SR beam formed by asymmetric Si(111) monochromator crystals passed through a system of slits, illuminated the sample right through, and excited the glow from the LuAG : Ce crystal scintillator. The scintillator was part of a recording system consisting of a mirror, an optical lens, and a detector. For the scintillator–CCD system, it is customary to give an optimized resolution value, which is obtained by dividing the average size of the effective pixels of the CCD matrix by the lens magnification. At  $20\times$  magnification, the optimized resolution is submicron.

## RESULTS AND DISCUSSION

Basal-faceted ribbons, as a rule, contain growth bands that repeat the shape of the crystallization front. They appear in the form of rows of gas pores in micrographs [1, 6] and topographs [15]. The analysis of topographs obtained earlier for ribbons showed that at the beginning of crystal growth, pores are the main structural defects, which are related to other defects,

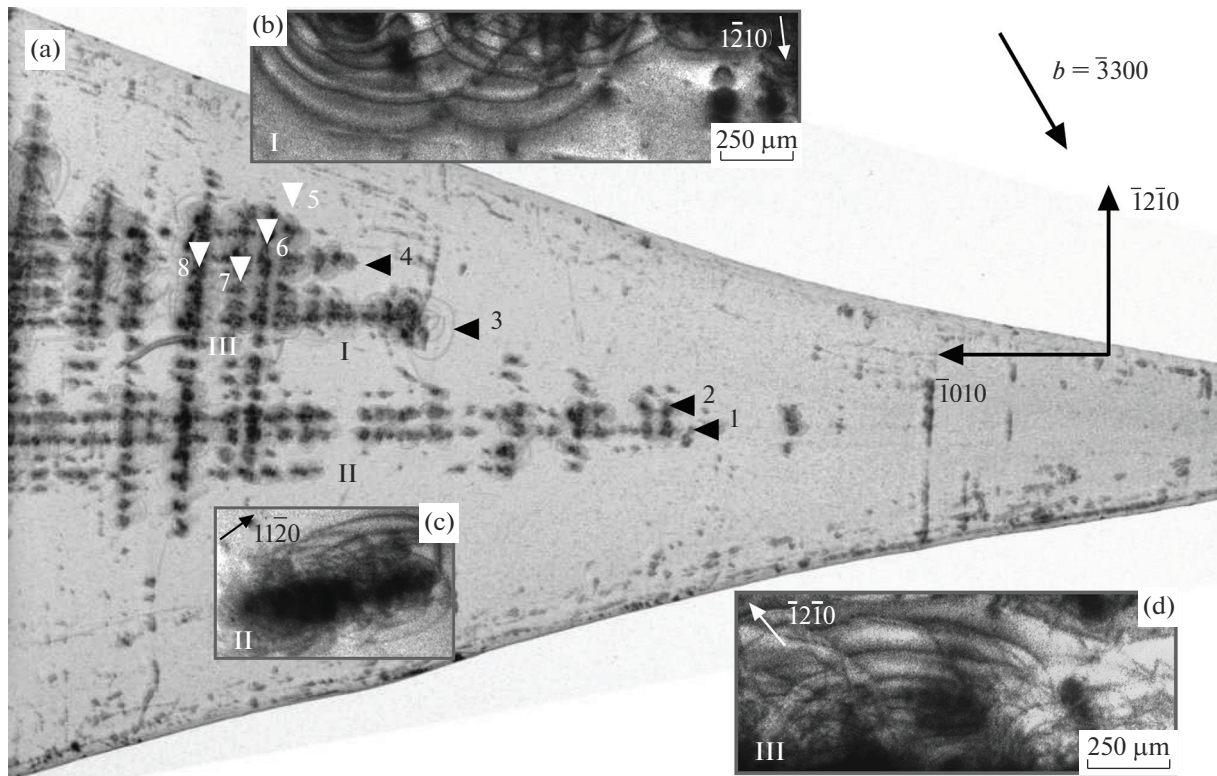


**Fig. 2.** (a) Lang projection topograph.  $AgK_{\alpha 1}$  is the radiation from an X-ray tube. Rows of dislocations and their sources parallel and perpendicular to the direction of growth of the ribbon  $[1010]$  are marked with black and white arrows with numbers (1)–(4) and (5)–(8), respectively. (b), (c), and (d) are enlarged images in synchrotron radiation ( $\lambda = 0.827 \text{ \AA}$ ) from sample areas marked on the projection topograph with numbers (I), (II), and (III). Fragment (d) is rotated around the normal to the image plane.

i.e., dislocations. According to earlier observations, the size of the pore images in the topographs increases with increasing ribbon length [15]. However, this does not occur due to an increase in the size of the pores themselves, but due to the generation of dislocation half-loops around them. The question of which properties of the pores themselves determine the generation of dislocations as the ribbon grows remains open.

It is quite obvious that an increase in the density of dislocations leads to overlapping of their images on the topographs. In transmission geometry, the upper limit of the dislocation density is  $\sim 10^4 \text{ cm}^{-2}$ . Above this limit, neither individual dislocations nor their sources can be distinguished. In the reflection geometry, when the absorption depth is small and X-ray radiation propagates only to a short distance into the crystal, the dislocation strain fields penetrating into the depth do not make a noticeable contribution to the images. It is generally accepted that the dislocation-density limit in this geometry is two orders of magnitude greater. However, there is no reason to assert that the sources are entirely located in a thin surface layer.

Let us also note that the use of transmission XRT methods has the advantage of shedding light on the problem of the formation of a block structure in the ribbons. On the one hand, within the framework of the

already existing block model [2, 3], a plane stress state occurs in thin, wide, basal-faceted ribbons and, as a consequence, the sliding of dislocations in the basal plane is difficult, and in the ideal case it is absent. On the other hand, the existence of basal dislocations in the ribbons was confirmed experimentally [15].

In this study, reflections from prismatic planes in the transmission geometry were used to analyze images of dislocations. The Lang projection topograph in Fig. 2a was obtained in the 3–300 reflection. The topograph shows the sample almost entirely. The seed is located on the right side of the image (not shown in the figure), in which there are no gas pores or dislocations. In the rest of the image one can see a configuration consisting of dislocation half loops, the nucleation centers of which are distributed in the form of rectilinear rows parallel and perpendicular to the direction of ribbon growth  $[1010]$ . The rows are marked with numbers from 1 to 4 and from 5 to 8, respectively. Some mass clusters of loops are marked with Roman numerals.

The large scale of the projection topograph does not allow details to be seen. Therefore, individual sections of the sample were examined using SR (Fig. 1b). Natural collimation in the vertical plane and horizontal slits limited the beam to  $\sim 25 \times 25 \text{ mm}^2$ . The topo-

grams were recorded on high-resolution Kodak M100 film at a distance of 15–20 cm from the sample. A Nikon universal optical microscope (Tokyo, Japan) with a 10 $\times$  objective lens and a CCD camera was used to magnify individual fragments of topographs.

In bulk sapphire single crystals, basal dislocations slide in the  $\langle 1\bar{2}10 \rangle$  directions [18]. They can be easily detected in ribbons in the  $\{1\bar{2}10\}$  reflections. In Figs. 2b–2d, the contrast from individual dislocations and from areas with a relatively low dislocation density is adjacent to images of dense clusters of highly curved lines. It is obvious that dislocations in tangles have different Burgers vectors. This distribution makes it difficult to estimate the average dislocation density. The absence of a dominant sliding pattern suggests that the tangles were formed under the influence of a non-directional stress field. The latter could arise as a result of thermal fluctuations or be caused by concentrators with complex configurations.

Under conditions of relatively low X-ray absorption  $\mu t = 1.8$ , direct images of the dislocations are bright [7]. The direct-image contrast is explained by a simple rule that is valid for screw and edge dislocations. The screw-dislocation contrast is zero when  $\mathbf{g} \cdot \mathbf{b} = 0$ , where  $\mathbf{b}$  is the Burgers vector of the dislocation, and  $\mathbf{g}$  is the diffraction vector. The edge-dislocation contrast is zero when, in addition,  $\mathbf{g} \cdot \mathbf{n} = 0$ , where  $\mathbf{n}$  is the normal to the sliding plane. Edge dislocations with Burgers vectors  $\langle 1\bar{2}10 \rangle$  sliding in the basal plane are visible on the topographs in the reflections from planes  $\{1\bar{2}10\}$ . However, the detectability of dislocations sliding in prismatic planes  $\{11\bar{2}0\}$  with Burgers vectors  $[1\bar{1}00]$ ,  $1/3[1\bar{1}01]$ , and  $1/3[20\bar{2}1]$  [19] requires additional analysis.

Figure 3a shows a phase-contrast image of the sample region shown in the previous Fig. 2a. The images of the gas pores form rows, which are highlighted with dotted lines similar to the previous figure. Some pores are irregular in shape, while others are spherical. The white arrow points to a group of small spherical pores spaced from clusters of larger pores. An enlarged image of spherical pores can be seen in Fig. 3b. Black arrows directed towards horizontal row 2 indicate a fragment with dimensions of  $\sim 0.4 \times 0.6 \text{ mm}^2$ . This fragment contains irregularly shaped pores formed due to some changed growth conditions (Fig. 3c). One should not think that the loss of spherical shape occurs abruptly; on the contrary, this change occurs gradually and is related to the fusion of pores with each other. The formation of spherical pores is fairly well explained [4–6], but the question of the nature of another type of pore continues to remain unclear, and there is the seed of the problem of dislocation generation.

By comparing the images obtained by the PCI and XRT methods, it is possible to establish a correspon-

dence between pores and dislocations. Spherical pores can be visible on synchrotron topographs due to the bipartite structure of the dynamic contrast [9, 10]. This is confirmed by our observations (data not shown). It turned out that pores of elongated and irregular shape did not appear on topographs despite their rather large size. Assuming that such pores always generate dislocations, we can conclude that their diffraction contrast is negligible compared to the contrast from tangles of dislocations. The conclusion suggests itself that the transformation of the pore shape is accompanied by the generation of dislocations.

Optical microscopy is used to determine the size of gas pores in sapphire [5, 6]. However, the large thickness of the ribbon ( $\sim 1 \text{ mm}$ ) makes it difficult to measure the diameter of small pores located deep in the crystal volume. The PCI method is equally applicable to both thin and thick samples. However, a complete description of the size and shape of pores can only be obtained by solving the inverse problem. Therefore, in this study, the computer simulation of images recorded on a detector at a precisely known distance from the sample was used.

Images were saved in the 16-bit Tag Image File Format (TIFF) with a spacing value for recording the number of photons from 0 to 65 535. In an experimental image of  $2560 \times 2160$  pixels (at  $Z_1 = 14 \text{ cm}$ ), the number of photons varies from 26 616 to 43 888. A fragment of  $490 \times 490$  pixels was cut out from the full image (Fig. 3b). As a result, the range became even smaller: from 35 738 to 41 615.

The contrast is equal to the difference between the maximum and minimum brightness of the image divided by the sum of these values. On the basis of the above, the contrast was quite weak:  $V = 0.076$ . At another distance  $Z_1 = 25 \text{ cm}$ , the contrast became slightly higher:  $V = 0.114$ . In other words, as the distance doubled, the contrast also doubled. This can be explained by the fact that in the near field, the contrast is determined by the local focusing and defocusing of radiation by the spherical surfaces of the pore. A quasi-parabolic decrease in thickness leads to focusing, and the opposite change leads to divergence of the beams. But the focal lengths are very long. And at the initial stage, this process linearly depends on the distance. Accordingly, the contrast also increases in the same way.

In addition, as the distance increases, the structure of the image consisting of shades of gray between the maximum and minimum intensity, which correspond to white and black, changes. Images of spherical pores have a simple structure consisting of a light center surrounded by a black ring. The size of the outer diameter, the width of the black ring, and the strength of the contrast are increased with distance from the sample. For  $Z_1 = 25 \text{ cm}$ , the diameter is equal to 50 pixels. Considering that the pixel size is 0.32 micrometers, we get 16 micrometers. On the basis of a spherical model

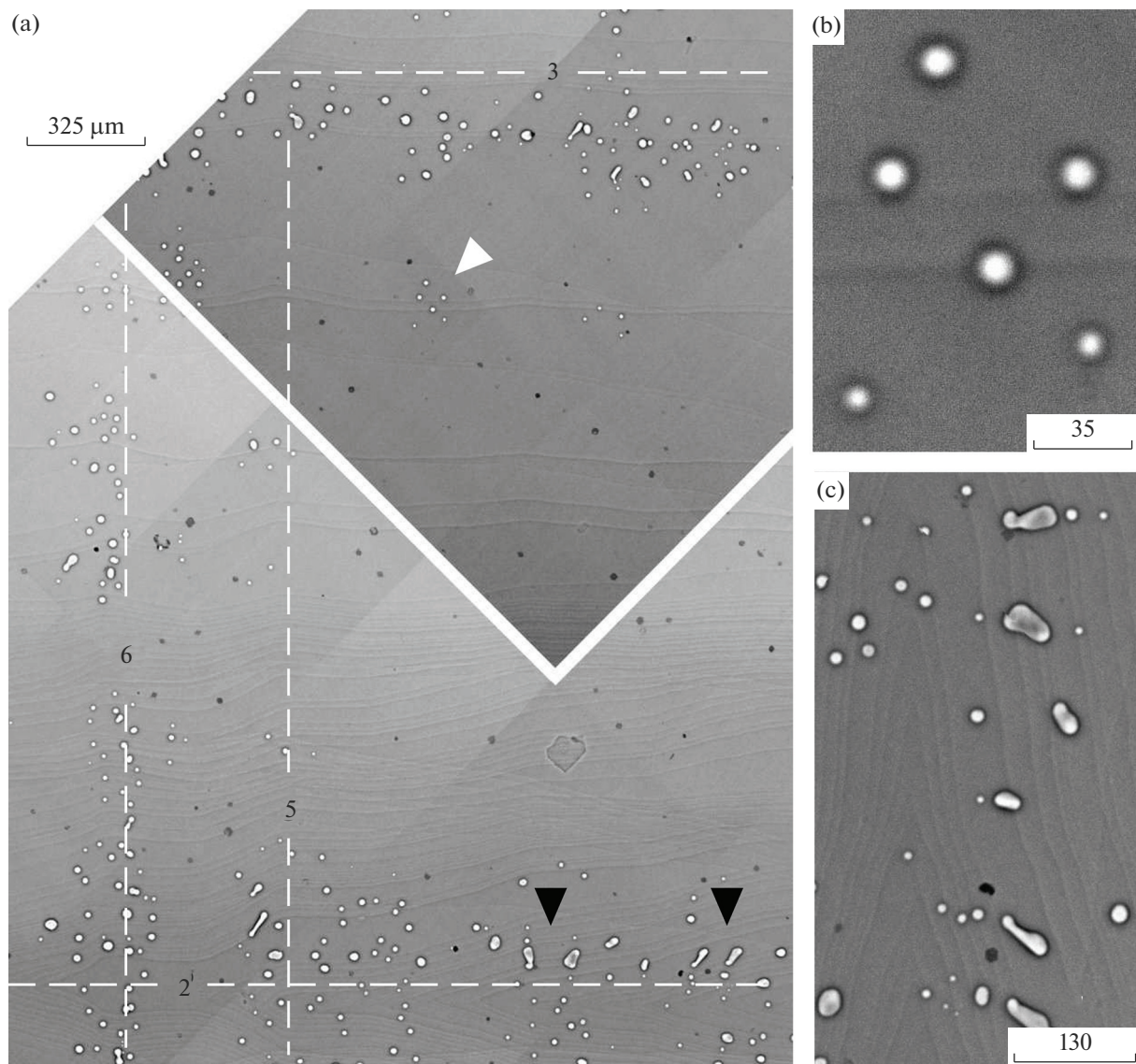


**Fig. 3.** (a) Phase-contrast image of that region of the sapphire ribbon that covers only rows (2), (3), (5), and (6) in Fig. 2a. The white arrow marks a group of small spherical pores. Black arrows highlight a fragment located in the second row of large pores irregularly shaped. (b) Enlarged image of spherical pores. (c) Enlarged view of irregularly shaped pores. Fragment (c) is rotated  $90^\circ$  around the normal to the image plane. The numbers near the scale bar are in micrometers.

with a diameter of  $16 \mu\text{m}$ , images of the pore at different distances  $Z_1$  were calculated. The calculation was carried out using the XRWP (X-ray Wave Propagation) program [20]. The program calculates a series of two-dimensional images in accordance with the formulas of the theory of phase-contrast images of 3D objects.

The propagation of radiation through a medium with variable electron density is described by the transmission function of the object. In this case, the thickness is a variable function of the coordinate, since the object is heterogeneous and contains voids inside it. The propagation of radiation in free space is calculated by the Huygens–Fresnel principle as the convolution

of the wave function with the Fresnel propagator [13, 14]. The convolution of the Fresnel propagator with the transmission function of the object was calculated by the fast Fourier transformation [21].

Simulation was performed for fully coherent monochromatic radiation from a point source and for an ideal detector. Good agreement with experimental images was achieved as a result of fairly strong averaging of the calculated picture. For averaging, the method of calculating the convolution of the intensity distribution at the detector for the fully coherent case with a Gaussian function of a given half width (FWHM) was used. Convolution was performed for different FWHM values, from which the value that

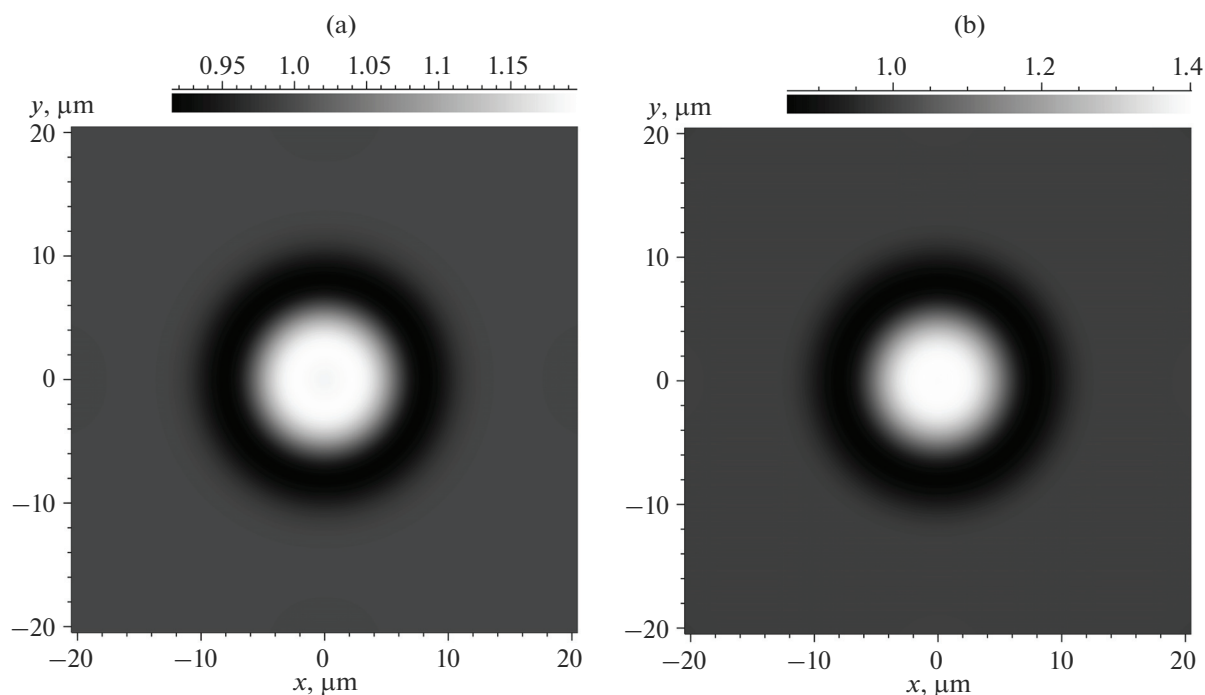


**Fig. 4.** Theoretical phase-contrast images of pores at distances of (a)  $Z_1 = 14$  cm and (b)  $Z_1 = 25$  cm. Calculation was carried out for the pore that is in the upper position in the group of pores in Fig. 3b.

best corresponded to the experiment was selected. The final FWHM was typically on the order of several micrometers.

Figure 4 shows the result of simulation. The contrast values of the calculated images were 0.133 and 0.241. These values are higher than the experimental ones. The latter observation can be explained by the fact that the detector records images along with the background. When comparing pore cross-sectional sizes, the background must be taken into account. To completely match the images characteristic of theory and experiment, a constant playing the role of the background was subtracted from the intensity recorded by the detector.

## CONCLUSIONS

The combination of XRT with the PCI method in synchrotron radiation contributes to progress in understanding the mechanisms of defect formation in basal-faceted sapphire ribbons. By sequentially placing the studied samples in conditions of diffraction reflection and phase-contrast imaging, it is possible to detect the correspondence between the contrast caused by the stress fields of structural defects and the phase contrast caused by gas pores. It was shown that gas pores with different sizes can have both spherical and more complex shapes.

The recording of phase-contrast images at different distances from the sample and computer modeling of the images made it possible to determine the diame-

ters of spherical micropores in the range from 10 to 20  $\mu\text{m}$ . These pores are not necessarily sources of dislocations. A surprising result is the fact that the transformation of the pore shape under the influence of altered growth conditions is directly related to the inhomogeneous distribution of dislocations. Dislocations of different sliding systems are present in places of accumulations of stress concentrators. In particular, the topographs obtained in reflections from prismatic planes show dislocations sliding in the basal plane.

The combination of XRT and PCI methods is especially relevant when studying the relationships between defect configurations, growth conditions, and physical properties of basal-faceted ribbons.

## ACKNOWLEDGMENTS

We are grateful to Dr. Sci. (Phys.-Math.) I. L. Shulpina (Ioffe Physical–Technical Institute, Russian Academy of Sciences) and Dr. Sci. (Phys.-Math.) M. Yu. Gutkin (Institute of Mechanical Science Problems, Russian Academy of Sciences) for participation in the discussion of the results.

## FUNDING

The study was carried out with financial support of the Ministry of Science and Higher Education of the Russian Federation. T. S. Argunova was supported by grant 075-15-2021-1349. V. G. Kohn was supported by grant 075-15-2021-1362.

## CONFLICT OF INTEREST

The authors declare that they have no conflicts of interest.

## REFERENCES

1. V. S. Yuferev, V. M. Krymov, L. L. Kuandykov, S. I. Bakholdin, Yu. G. Nosov, I. L. Shulpina, and P. I. Antonov, *J. Cryst. Growth* **275**, e785 (2005). <http://doi.org/10.1016/j.jcrysgro.2004.11.094>
2. P. I. Antonov, V. M. Krymov, Yu. G. Nosov, and I. L. Shul'pina, *Izv. Ross. Akad. Nauk, Ser. Fiz.* **68**, 777 (2004).
3. L. Kuandykov, S. Bakholdin, I. Shulpina, and P. Antonov, *J. Cryst. Growth* **275**, e625 (2005). <http://doi.org/10.1016/j.jcrysgro.2004.11.040>
4. I. Nicoara, O. M. Bunoiiu, and D. Vizman, *J. Cryst. Growth* **287**, 291 (2006). <http://doi.org/10.1016/j.jcrysgro.2005.11.032>
5. A. V. Borodin, V. E. Kamynina, D. N. Frantsev, and M. V. Yudin, *Crystallogr. Rep.* **54**, 669 (2009). <https://doi.org/10.1134/S106377450904021X>
6. A. V. Borodin and V. A. Borodin, *J. Cryst. Growth* **478**, 180 (2017). <http://doi.org/dx.doi.org/10.1016/j.jcrysgro.2017.08.028>
7. A. R. Lang, *Diffraction and Imaging Techniques in Material Science*, Ed. by S. Amelinckx, R. Gevers, and J. Van Landuyt (North-Holland, Amsterdam; Metallurgiya, Moscow, 1984).
8. I. L. Shul'pina, E. V. Suvorov, I. A. Smirnova, and T. S. Argunova, *Tech. Phys.* **67**, 1277 (2022). <http://doi.org/10.21883/TP.2022.10.54354.23-22>
9. T. Tuomi, *J. Synchrotron Radiat.* **9**, 174 (2002). <http://doi.org/10.1107/S0909049502004284>
10. K.-P. Gradwohl, A. N. Danilevsky, M. Roder, M. Schmidbauer, J. Janicsko-Csathy, A. Gybin, N. Abrosimov, and R. Sumathi, *J. Appl. Cryst.* **53**, 880 (2020). <http://doi.org/10.1107/S1600576720005993>
11. L. Mancini, E. Reinier, P. Cloetens, J. Gastaldi, J. Hartwig, M. Schlenker, and J. Baruchel, *Philos. Mag. A* **78**, 1175 (1998). <http://doi.org/10.1080/01418619808239982>
12. S. Agliozzo and P. Cloetens, *J. Microsc.* **216**, 62 (2004). <http://doi.org/10.1111/j.0022-2720.2004.01385.x>
13. T. S. Argunova and V. G. Kohn, *Phys.—Usp.* **62**, 602 (2019). <http://doi.org/10.3367/UFNe.2018.06.038371>
14. A. Snigirev, I. Snigireva, V. Kohn, S. Kuznetsov, and I. Schelokov, *Rev. Sci. Instrum.* **66**, 5486 (1995). <http://doi.org/10.1063/1.1146073>
15. I. L. Shul'pina, S. I. Bakholdin, V. M. Krymov, and P. I. Antonov, *Bull. Russ. Acad. Sci.: Phys.* **73**, 1364 (2009).
16. T. S. Argunova and V. G. Kohn, *Materials* **15**, 856 (2022). <http://doi.org/10.3390/ma15030856>
17. P. A. Prosekov, V. L. Nosik, and A. E. Blagov, *Crystallogr. Rep.* **66**, 867 (2021). <http://doi.org/10.1134/S106377452134006X>
18. J. M. Lommel and M. L. Kronberg, *Proc. Conf. "Direct Observation of Imperfections in Crystals,"* Ed by J. B. Newkirk and J. H. Wernick (Interscience, 1962), p. 543.
19. Y. Takano, K. Kohn, S. Kikuta, and K. Kohra, *Jpn. J. Appl. Phys.* **9**, 847 (1970). <http://doi.org/10.1143/JJAP.9.847>
20. V. Kohn, <http://xray-optics.ucoz.ru/XR/xrwp.htm>.
21. J. W. Cooley and J. W. Tukey, *Math. Comput.* **19**, 297 (1965).

*Translated by S. Rostovtseva*

**Publisher's Note.** Pleiades Publishing remains neutral with regard to jurisdictional claims in published maps and institutional affiliations.

SPELL: 1. OK